JTTEE5 10:267-284

Controlling Particle Injection in Plasma Spraying

M. Vardelle, A. Vardelle, P. Fauchais, K.-I. Li, B. Dussoubs, and N. J. Themelis

(Submitted 23 May 2000)

This paper reviews experimental and analytical techniques that examine the efficiency of systems for the injection of powders in plasma jets used in spray coating. The types of injectors, the experimental techniques for observing particle trajectories and distributions, and the mathematical models used to investigate the momentum and heat-transfer phenomena between particles, carrier gas, and plasma jet are described. Experimental data are presented from numerous examples from the plasma spraying of ceramic powders.

Keywords diagnostic techniques, injection control, modeling, particle injection

1. Introduction

The coating of surfaces by plasma spraying is an important manufacturing process with many industrial applications.[1,2] The process parameters required to produce sound and reproducible coatings are usually specified in terms of controllable parameters associated with the spray equipment, such as arc current, plasma gas composition, and flow rate and "stand-off" distance. They are typically based on experiment and/or experience. However, robust and easy-to-use optical sensors have now been developed on the basis of fundamental studies of the behavior of particles within the plasma jet and at impact.[3–14] These sensors are used to measure particle temperatures, velocities, and trajectories.

In operation, the plasma torch can be moved in front of the sensor head for about 1 min. After the piece is coated, the torch comes back in front of the sensor head for another 1 min measurement. This procedure allows the operator to check for any drift in particle parameters that may affect the quality of the coating. Such a setup can be used to compare torches working with the same operating parameters in different spray booths, estimate the time necessary for reaching stable particle spraying conditions, and generally improve the performance and reproducibility of the plasma spray process.

Experimental studies with such sensors have shown the importance of injector geometry and carrier gas flow rate on the particle trajectory. For a given particle morphology and size distribution, particle trajectory within the plasma jet determines particle temperature and velocity at the point of impact with the substrate; this, in turn, controls the thermomechanical properties of the coating.[15–17] The effect of the injector system on the acceleration and heating of sprayed particles has been studied extensively both experimentally and analytically. This paper is a review of this work and it encompasses (1) the effect of straight and curved injectors and their positioning; (2) a discussion of the optical sensors used to observe the injection of particles and their trajectories in the plasma jet; (3) a commentary on the mathematical models developed for the analysis of the particle dynamics at the injector exit, the influence of the powder/carrier gas flow on the plasma jet, and the momentum and heat-transfer phenomena as the particle travels through the jet; and (4) examination of stability of particle injection.

M. Vardelle and **P. Fauchais,** University of Limoges, Laboratory "Sciences des Procédés Céramiques et de Traitements de Surface," 87060 Limoges Cedex, France; **A. Vardelle,** ENSIL, Laboratory "Sciences des Procédés Céramiques et de Traitements de Surface," 87068 Limoges Cedex, France; and **K.-I. Li,** MADYLAM , 38402 Saint Martin d'Hères Cedex, France; **B. Dussoubs,** Ecole Nationale Supérieure des Mines de Nancy - LSG2M, 54042 NANCY Cedex, France; and **N. J. Themelis,** Earth Engineering Center, Columbia University, New York, NY 10027. Contact e-mail: fauchais@unilim.fr.

2. Powder Injection Techniques

2.1 Feed Materials

The commercial grade ceramic powders discussed in this paper are representative of powders used in plasma coating. Two types of zirconia, partially stabilized with 8% yttria (Table 1), are referred to as (1) Starck zirconia powder, product ID 825 (Starck GmbH & Co. KG., Germany), produced by fusing and grinding, sieved to four size distributions; and (2) Sulzer-Metco zirconia powder, product ID 7592 (Sulzer Metco (US) Inc., Westbury, NY), produced by spray drying, agglomeration, and sintering. This powder was sieved into three fractions, referred to in this paper as the "fine," "medium," and "coarse" powders.

The Starck powder particles were angular and fully dense, while most of the Sulzer-Metco powders consisted of spherical particles and contained a large amount of fines, probably generated by unagglomerated precursor materials. In addition, the various batches exhibited different densities due to the variety of internal microstructures formed during the manufacturing process. The fine powder contained a significant fraction of fully densified particles, while larger particles were porous with different internal porosities. The higher density of the coarse fraction is due to the skeleton-like morphology of the particles that facilitated the penetration of helium atoms into the material during the density measurements.

Fused and crushed Al_2O_3 and Cr_2O_3 powders were also used with size distributions, respectively, of 5 to 22 μm and 22 to 45 μm. Both of these powders were angular and fully dense. The

Nomenclature

d_p	particle diameter, m
f	focal length of a lens, mm
L	straight length of curved injectors, mm
L_e	minimum length for the complete development of velocity profile in a tube, m
L_1, L_2	lens
P	electric power, W
P_{eff}	effective electric power, *W*
r	radial coordinate, *m*
R	radius of curvature of curved injectors, mm
Re	Reynolds number, Re = $\rho_g d_p u/\mu_g$
R_{inj}	radius of injector, m
R_t	radius of the plasma torch nozzle, m
Sc_t	turbulent Schmidt number, ratio of momentum diffusivity to molecular mass diffusivity
t_r	particle residence time, s
T	temperature, K
T_a	anode wall temperature, K
T_{max}	maximum plasma gas temperature at the nozzle exit, K
u	velocity, $m \cdot s^{-1}$
u_m	average velocity, $m \cdot s^{-1}$
u_{max}	maximum plasma gas velocity at the nozzle exit, $m \cdot s^{-1}$
μ_g	gas viscosity, $kg \cdot m^{-1} \cdot s^{-1}$
ρ_p	density of particle material, $kg \cdot m^{-3}$
ρ_g	plasma gas density, $kg \cdot m^{-3}$

Table 1 Size distribution and density of the powders used in this study

		Mean diameter (μm)	Standard deviation (μm)	Density (kg/m^3)	Condition
ZrO_2	Starck	72	9	5700	1
	powder	36.2	11.1	5700	2
		14	7.5	5700	3
		27	19	5700	4
Sulzer	Fine powder	37.8	19.2	4752	5
Metco	Medium powder	53.5	21.3	5058	6
	Coarse powder	93.6	24.3	5325	7
	Ensemble	67.3	33.2	4952	8
Al_2O_3	Starck powder	33.2	11.1	2900	9
Cr_2O_3	Starck powder	14	7.5	5200	10

iron particles used in one test were of spherical shape and of size distribution 14 to 45 μm.

2.2 Powder Feeder

Vibrating screw feeders were used to provide a constant mass flow of powder, usually set at 1 kg/h, for all types of powders. This flow is chosen to ensure that there are no overload effects either in the injector or within the plasma jet, even when feeding very fine particles (<10 μm).

2.3 Carrier Gas

The carrier gas imparts to the powder particles sufficient momentum to penetrate into the plasma jet so that they become entrained in the plasma gas. Therefore, in nearly all applications, the carrier gas is of relatively high density, such as argon or nitrogen.

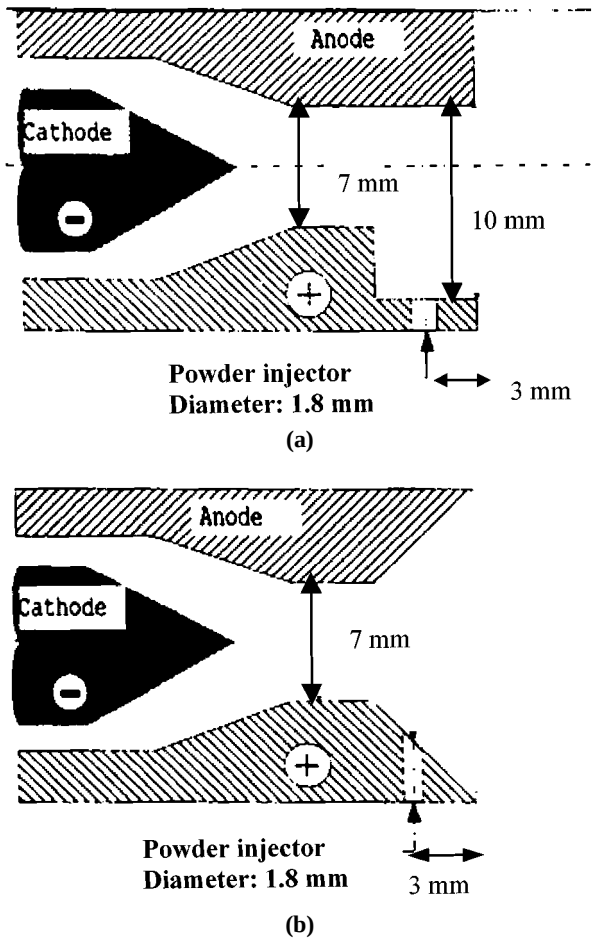

Fig. 1 (**a**) and (**b**) Schematic diagrams of internal injection with two types of design to facilitate the escape of carrier gas

2.4 Position of Powder Injectors

The powder injection device can be located either inside the nozzle of the plasma torch (internal injection, Fig. 1) or at a very short distance downstream of the plasma torch exit (external injection). Internal injection offers the advantages of precise location of the injector and more inclusive heating of the entire spectrum of particle sizes,[6] but it also introduces a significant perturbation in the plasma jet flow. With external injection, the position of the injector tip is not as well defined, but it is easier to control the injection parameters and to maintain the injector.

2.5 Injector Geometry

Two commonly used injectors consist of a straight tube or a 90° curved tube with various radii of curvature, *R*, followed by a straight section, *L*. These two geometries were compared by testing two stainless steel injectors of inside and outside diameters 1.75 and 3.17 mm, respectively. The schematic diagrams of

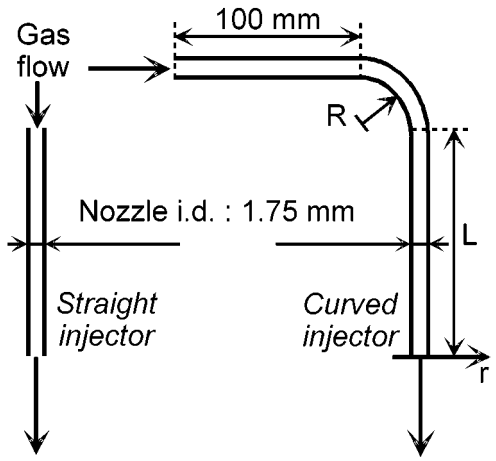

Fig. 2 Geometry of two types of injectors used in this study

Table 2 Radius of curvature, *R*, and straight length, *L*, of curved injectors

Curvature *R*, mm	Length *L*, mm
12.7	35.0
25.4	35.0
25.4	101.6
25.4	203.2
50.8	35.0

these injectors are shown in Fig. 2, and the various values of *R* and *L* are listed in Table 2. The flexible powder feed tube linking the powder feeder and the injector was about 1.5 m long.

Other internal diameters (between 1.5 and 2 mm) of straight injectors have also been tested. A two-port injector has been investigated, where the powder was injected through two injectors with internal diameters of 1.5 and 1.8 mm (Fig. 3a). Another type of injector, called the "double flow injector," was also examined, both in cold flow tests and under plasma flow conditions (Fig. 3b). The double flow refers to a "shroud" of gas flowing through a tube concentric to a conventional powder injector. The annulus between the two cylinders plus the cross-sectional area of the inner tube amount to an effective cross-sectional surface area of 2.8 mm^2, which is very close to that of a conventional 2 mm diameter injector.

3. Techniques of Observation

3.1 Particle Distribution at Injector Exit

The radial distribution of number of particles exiting from the injector nozzle has been determined by directing the particle flow exiting from the injector against an adhesive tape and measuring the resulting particle distribution stuck on the tape *via* microscopy. A layer of the tape was applied to a thin steel plate (51 × 51 × 3.2 mm thick) and covered by copper foil (0.075 mm), which had an aperture of 17.5 mm. A plexiglas disc, containing an aperture of 19 mm diameter, was located between the injector and the sample coupon. The disk was spun at a peripheral velocity of about 0.16 m/s, yielding a spray deposition time

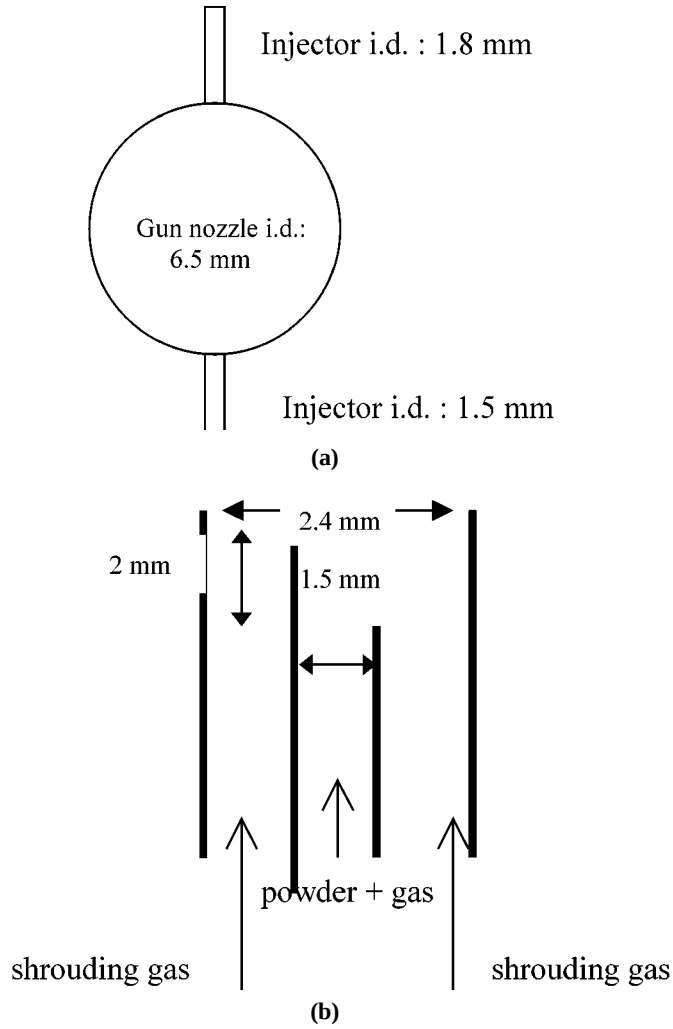

Fig. 3 (**a**) Injection of powder through a two-port injector. (**b**) Schematic of double flow injector

of 100 ms. Eleven experiments were conducted at axial distances of 17, 34, and 50 mm from the injector. The parameters of the various tests are listed in Table 3.[18]

Examination of the spatial distribution of the particles collected in the above tests did not show any clear trend of particle size segregation for either of the zirconia powders or for the two types of injectors. All samples exhibited a visually uniform distribution for both small and large particles. The computed particle distributions were in fair agreement with these observations for the straight injector, whereas for the curved injectors, the computed spray patterns at the exit were narrower than the observed ones. This discrepancy may be due to the increase in mass loading in the outer region of the curve; *i.e.*, the ensuing particle-particle collisions help scatter the particles throughout the entire cross section of the tube.

3.2 Particle Trajectories using Laser Scattering

The trajectories of injected particles can be observed by focusing a laser beam through the particle/gas jet and using a pho-

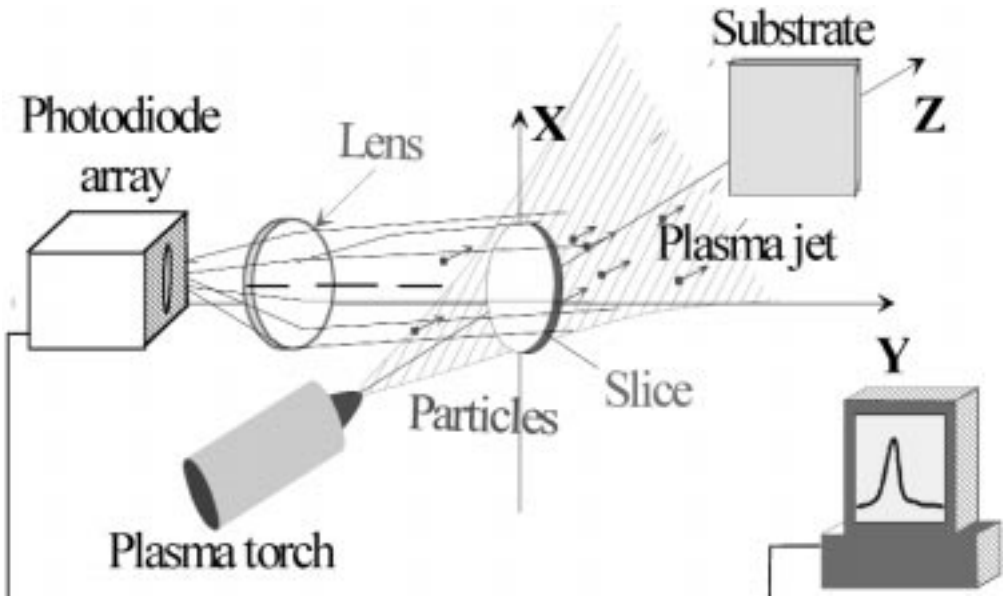

Fig. 4 Schematic view of apparatus for determining hot particle trajectories

Table 3 Injection conditions for experiments on particle size segregation

Powder type	Injector type	Stand-Off distance(a), mm
Starck	Curved	17
Starck	Curved	17
Starck	Curved	34
Starck	Straight	17
Starck	Straight	34
Sulzer Metco	Straight	17
Sulzer Metco	Straight	17
Sulzer Metco	Straight	34
Sulzer Metco	Curved	34
Sulzer Metco	Curved	17
Sulzer Metco	Curved	50

(a) The stand-off distance is the distance between the exit of the injector and the surface of the sample coupon

toelectric detector to measure the bursts of scattered light as the particles flow past the laser beam. A uniform laser sheet is generated at a right angle to the jet flow by an oscillating mirror (2400 Hz). The light beam is produced by a 2 W argon ion laser. It passes through a focusing lens, L_1 (f = 210 mm), onto the oscillating mirror, and is focused at the centerline of the torch. A second lens, L_2 (f = 210 mm), is used to collect the light scattered by the particles and to focus it through a slit and then onto a photo-diode array connected to a computer for data acquisition. The monochromator is adjusted at the source laser wavelength (514.5 nm) and filters the incoming optical signals with a band-pass less than 0.1 nm.

3.3 Particle Trajectories Using Thermal Radiation

A schematic diagram of the experimental setup used to detect the thermal radiation emitted by the heated particles in a plasma jet is shown in Fig. 4. In this case, the laser beam is turned off and the lens L_2 focuses the light emitted by the particles onto a monochromator. The band pass is now set at 3 nm so to eliminate the emission lines of the plasma gas. The time sequence for data acquisition is 13 ms, which allows the recording of 70 spectra per second, or a time-averaged recording, over periods of 0.013 to 120 s. The data processing consists of substracting the background light and determining the maximum amplitude and its position along the plasma jet radius. The amplitude of the light signals depends both on the number of particles and their temperature and provides information about the hot particle density and their mean trajectory.

For a fixed set of plasma torch conditions, the comparison of these data with stored reference data enabled corrective actions to be made when a drift was observed. Typical signals obtained within the plasma jet at different distances x from the nozzle exit are shown in Fig. 5(a), which shows the radial distribution of hot particles observed with the laser turned off, and the total particles distribution, as observed by means of the scattered laser beam.

In order to obtain a noise-free signal of the overall injected particle distribution profile, a mathematical subtraction technique was applied to eliminate the light intensity contributions from the plasma jet and the radiation from the hot particles. The resulting hot and cold particle distribution profiles are shown in Fig. 5(b).

3.4 Other High-Temperature Observation Systems

Moreau *et al.*[11,12] have measured simultaneously particle temperatures by means of a two-color pyrometer and particle velocities by a time-of-flight technique. An optical fiber linear array, located within the same sensor head, is used to monitor the particle jet and characterize the trajectories of the sprayed particles. The radiation from the hot particles is recorded by a camera and allows measurement of the orientation and width of the particle jet relative to the plasma torch. The corresponding di-

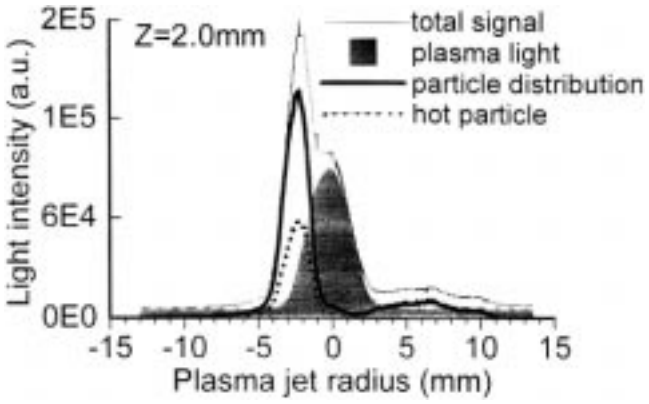

(a)

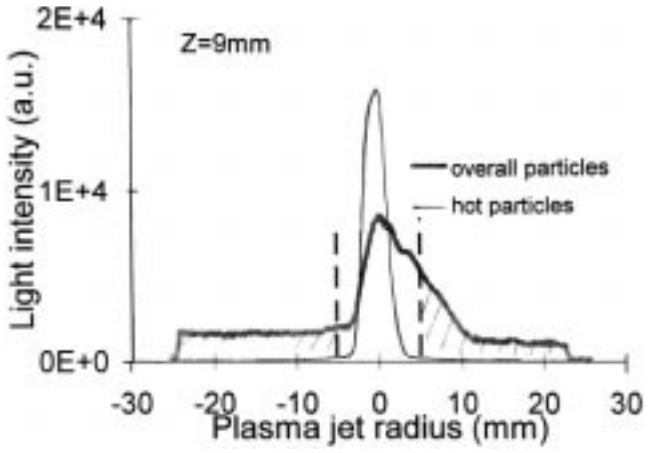

(b)

Fig. 5 (**a**) Typical light signals in plasma spraying (zirconia particles, 22 to 45 μm, 0.5 kg/hh, plasma gun i.d. 7 mm, 45 slm Ar, 15 slm H_2, I = 600 A, and V = 77 V). (**b**) Distribution profiles of hot and cold particles (iron particles, 14 to 45 μm, 0.5 kg/h, plasma gun i.d. 7 mm, I = 880 A, V = 60 slm Ar, and V = 32 V)

mensions of the measurement volume were about 3.9 mm length $\times$ 380 μm height $\times$ 500 μm width.

A similar but simpler system has been developed by Swank *et al.*[13] The sensor head forms a pencil-shaped measurement volume (approximately 5 mm diameter $\times$ 50 mm length) and measures, by means of two-color pyrometry, the mean temperature of the particles passing through this volume. This system has been used to observe the effect of varying the process input parameters (arc current, carrier gas flow rate, and plasma gas flow rate) on particle mean temperature and velocity. The latter is measured by laser anemometry.[19–21]

4. Mathematical Modeling of Jet and Particle Flow

The momentum transfer from the carrier gas to the injected particles and the momentum/heat-transfer phenomena within the plasma jet, with and without particle injection, have been modeled using the commercial simulation software Estet-Astrid (Simulog, Guyancourt, France). The software solves the conservation equations of mass, momentum, and energy for steady or unsteady, compressible, turbulent flow[18,22,23] in two- or three-dimensional domains.

The developed models are based on the following prime assumptions:[24–26] (1) steady and turbulent flow—turbulence is modeled by the standard k-ε model, used with a correction for low Reynolds numbers[27] in the potential core of the jet and close to walls; (2) plasma is in local thermal equilibrium and optically thin; (3) particle trajectories are computed using a Lagrangian scheme; (4) particle dispersion due to turbulence is taken into account; (5) interactions of particles with the injector walls are considered; and (6) interactions between particles are neglected. With regard to the last assumption for a powder feed rate of 1 kg/h and the carrier gas flow rates used in this study, the mean distance between two particles in the injector is approximately 10 times the particle mean diameter. Therefore, this assumption is valid for particles following linear trajectories but may not be valid for curved injectors, as was discussed earlier.

4.1 Gas Flow within Injector

For an argon gas flow of 3 to 8 slm, the Reynolds number in a 1.75 mm i.d. injector ranges from 3000 to 8000. The transition from laminar to turbulent starts at about Re > 2100 and is considered to become fully turbulent at Re > 4000. If it is assumed that the flow within a straight injector is turbulent, the velocity distribution $u(r)$ is expressed by

$$u(r) = \frac{u_m}{0.875}\left(1 - \frac{r}{R_{\text{inj}}}\right)^{1/7} \quad \text{(Eq 1)}$$

where u_m is the average velocity determined from the gas flow rate and R_{inj} the radius of the injector.

Computations of the gas flow through various curved injectors showed that the streamlines are distorted toward the outer periphery of the curvature and are reestablished in the straight portion of the tube after the curvature. As a result, the computed gas velocity profiles at the exit were similar both for straight and curved injectors. For turbulent flow, the minimum length, L_e, necessary for the complete development of the velocity profile in the tube can be estimated from[28]

$$L_e = 8.8\,\text{Re}^{1/6}\,R_{\text{inj}} \quad \text{(Eq 2)}$$

For 3000 <Re < 8000, this relationship yields an L_e ranging from 29 to 34 mm and is within the range of straight sections following curved injectors, as discussed earlier. This calculation supports the conclusion that the particle/gas exiting from a curved injector of L > 35 mm is not affected by the presence of curvature.

4.2 Gas/Particle Flow in Straight Injector

Figure 6(a) shows the distribution of zirconia particles (Table 1, tests 5 to 7) as a function of the injector radius.[29] It can be seen that the small particles (test 5) have a tendency to "tilt" to-

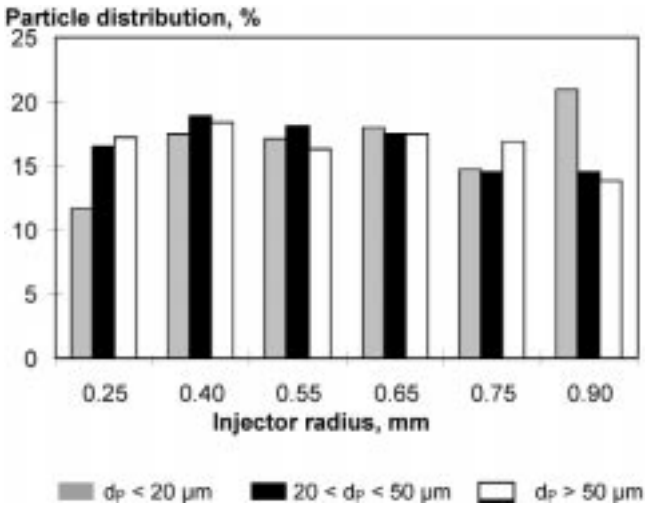

(a)

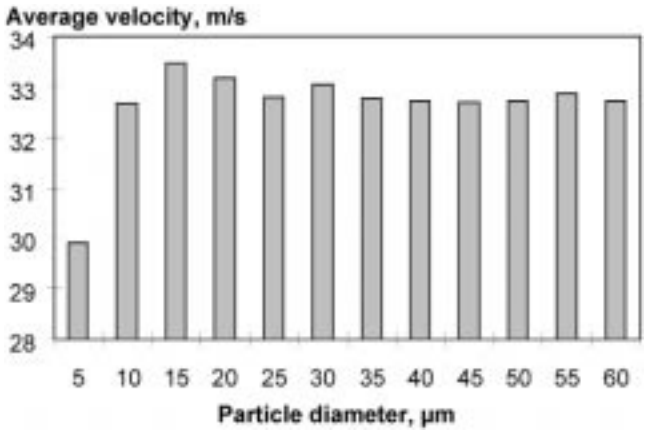

(b)

Fig. 6 (**a**) Particle distribution at injector exit as function of particle size. (**b**) Particle mean injection velocity as function of particle diameter and injector radius

ward the injection wall, due to turbulent dispersion, and they lose part of their energy when hitting the tube wall. This results in a lower velocity (Fig. 6b). Such fine particles have a low momentum and have difficulty penetrating the plasma jet at the injection point. For particles larger than 20 μm, the particle velocity is not affected much by particle size (Fig. 7[18]). The zero value on the bottom curve of Fig. 7 indicates particles that would be preferentially segregated to the wall.

As shown in Fig. 8(a),[30] a change in carrier gas flow rate from 4 to 6 slm (a typical range used in plasma spraying) has little effect on the dispersion of zirconia powders of 22 to 45 μm size. However, for finer particles (5 to 22 μm; test 3, Table 1), the diameter of the particle spray jet increases with carrier gas flow rate (Fig. 8b). This behavior arises because the fine particles follow the carrier gas flow more readily and the frequency of particle collisions with the injector inner wall has more effect for smaller particles. These results are in good agreement with experimental observations.

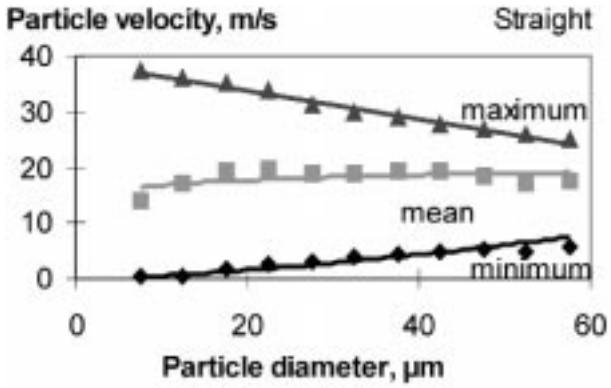

Fig. 7 Computed particle velocity vs diameter for ZrO_2 powder (tests 5 to 7, Table 1) straight injector; carrier gas flow rate: 4 slm, and L = 35 mm

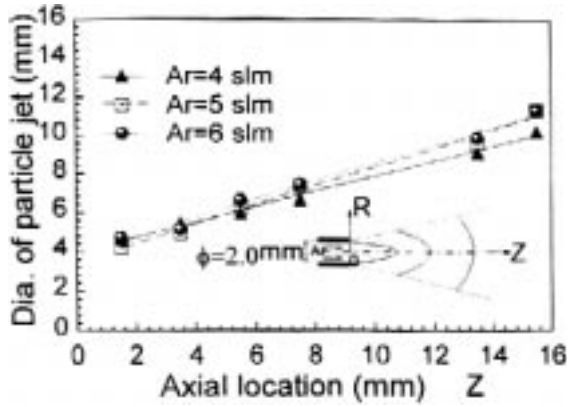

(a)

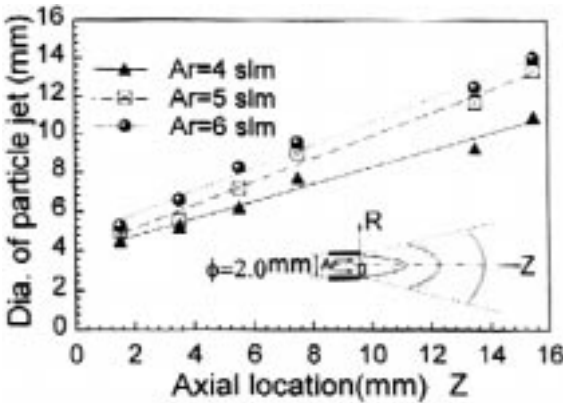

(b)

Fig. 8 Evolution of diameter of gas/ZrO_2 particle jet with axial distance from the injector exit: (**a**) 22 to 45 μm (test 2, Table 1); (**b**) 5 to 22 μm (test 3, Table 1) (carrier gas flow rate: 4 slm, and R = 12.7 mm)

4.3 Gas/Particle Flow in Curved Injector

The geometry of the curved injector has a greater effect on particle behavior. As the particles approach the bend, they decelerate and are driven to the outer regions of the bend due to the

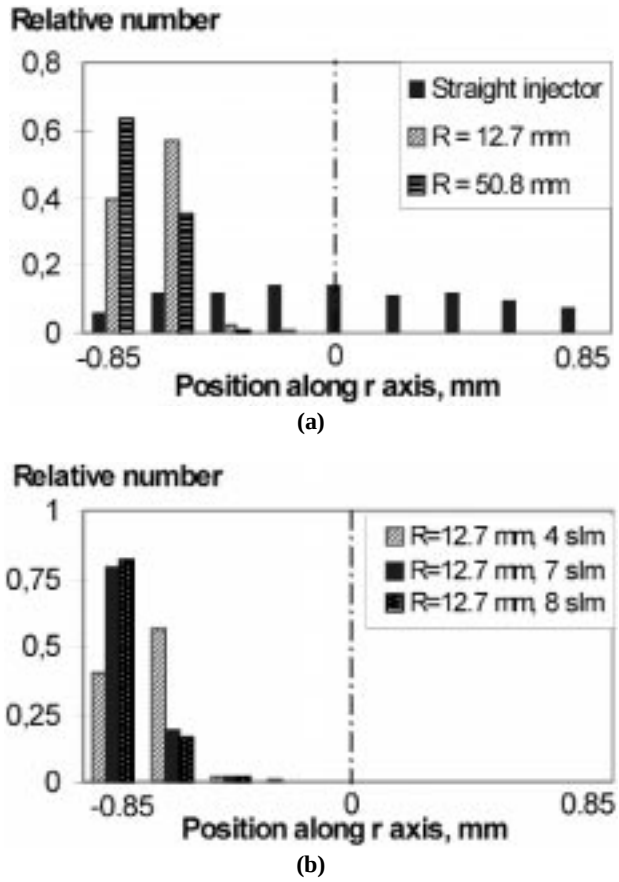

Fig. 9 Computed number of zirconia particles (test 2, Table 1) along the diameter of the injector at its exit (the -*r* coordinate denotes the outer part of the curvature): (**a**) various injector geometries and (**b**) various gas flow rates, curved injector

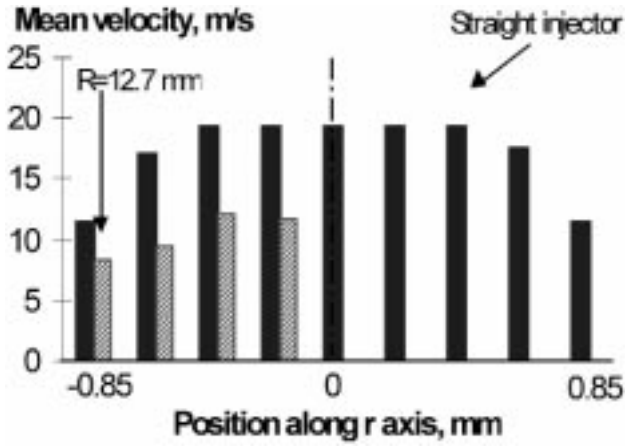

Fig. 10 Computed particle mean velocity along the diameter of the injector at the exit point (the -*r* coordinate denotes the outer half of the curvature); carrier gas flow rate: 4 slm, zirconia powder (test 2, Table 1)

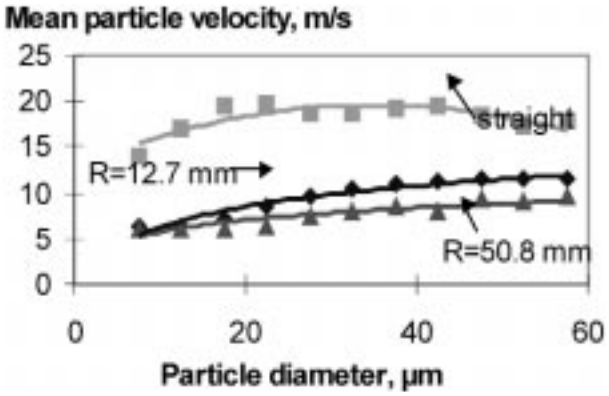

Fig. 11 Computed mean particle velocity vs particle diameter for ZrO_2 powder injected in the different tubes; carrier gas flow rate: 4 slm, and L = 35 mm

centrifugal forces imparted by the flow. In this zone, the gas has a lower velocity, resulting in a decrease in the drag force exerted on the particle by the enveloping fluid. Figure 9(a)[18] shows the relative number of zirconia particles (test 2, Table 1) along the radius in the plane of the curvature for different injector geometries and a carrier gas flow rate of 4 slm; Fig. 9(b) shows the particle distribution in a curved injector (R = 12.7 mm) for different gas flow rates.

Figure 10[18] compares the computed radial distribution of particle mean velocity at the exit of a straight and a curved injector (R = 12.7 mm). Over 90% of the particles are concentrated in the outer part of the curvature, while in the straight injector, particles have a more uniform distribution similar to the flat velocity profile of turbulent gas flow.

Figure 11[18] shows the computed change in velocity profile with particle size for both types of injectors. Again, it can be seen that particle diameters over 20 μm have little influence on particle velocity. As illustrated in Fig. 11, the particles are driven to the outside of the curvature, where the gas velocity is lower and collisions with the wall are enhanced. Changing the curvature of the bend has little effect on the particle mean velocity. An analytical study[31] has also shown that the angle of curvature has a greater effect on particle velocity than its radius. The above predictions are in good agreement with the experimental results of Fincke *et al.*,[21] which showed little dependence of particle velocity on particle size at the injector exit.

4.4 Effect of Gas/Powder Injection on Plasma Jet

In the Estet fluid dynamics program, the mass diffusion of species is assumed to behave similarly to heat diffusion; *i.e.*, the effective diffusivity of each species is equal to its thermal diffusivity. In addition, the Schmidt turbulent number, Sc_t (the ratio of momentum diffusivity to molecular mass diffusivity), is fixed at 0.7.[32] The thermodynamic and transport properties of the gas mixture, consisting of the plasma-forming gas, the carrier gas, and the ambient atmosphere, are determined on the basis of the laws of mixtures and the properties of pure argon, air, and argon-hydrogen mixtures.[33]

A rectangular mesh is used, subdivided into a nonuniform $49 \times 49 \times 43$ grid. The length of the calculation domain is 100 mm and its radius of 21 mm is about 7 times the radius of the nozzle torch. At the two inlets of the domain, *i.e.*, at the plasma torch and injector exits, the values of all variables are defined. At the plasma torch exit, the following profiles are used for the

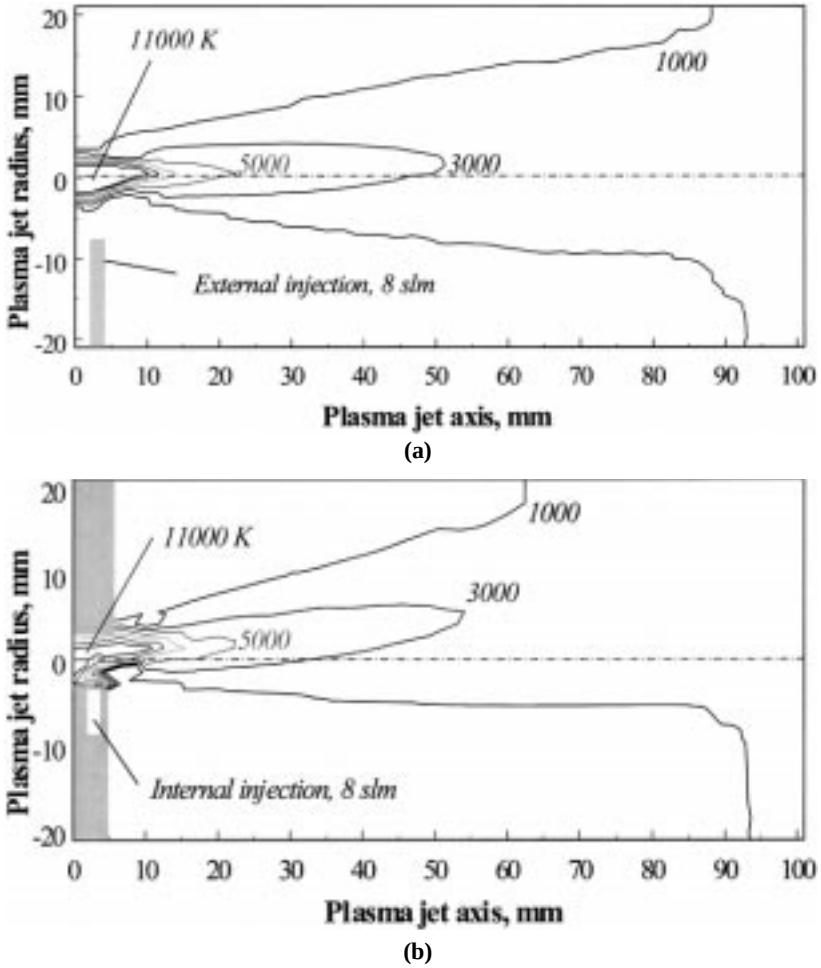

Fig. 12 (**a**) Isothermal lines at intervals of 2000 K for powder external injection (plasma forming gas: 27 slm Ar + 7 slm N_2; carrier gas flow rate: 8 slm; I = 600 A, V = 65 V, ρ = 56%; and plasma gun i.d. 6 mm). (**b**) Isothermal lines at intervals of 2000 K for powder internal injection (same conditions as in a)

temperature and the axial component of velocity, after Chang and Ramshaw:[34]

$$T = (T_{\max} - T_a)\left(1 - \left(\frac{r}{R_t}\right)^{4.5}\right) + T_a \quad \text{(Eq 3)}$$

$$u = u_{\max}\left(1 - \left(\frac{r}{R_t}\right)^{2}\right) \quad \text{(Eq 4)}$$

where $u_{\max}$ and $T_{\max}$ are the velocity and temperature of the plasma jet at the torch axis, T_a is the temperature of the anode, set to 700 K, and R_t is the plasma torch radius; $u_{\max}$ and $T_{\max}$ are computed from the enthalpy and mass flow rate at the plasma torch exit.

The effect of the powder carrier gas is more noticeable for internal injection, as can be seen by comparing the computed data of Fig. 12(a) and (b).[35] In these tests, the plasma forming gas is a mixture of 27 slm of argon and 7 slm of hydrogen and the carrier gas flow 8 slm of argon; the effective power dissipated in the gas is 13 kW, the plasma torch i.d. 6 mm, and the injector i.d. 1.6 mm. Under these conditions, the angles of the plasma jet axis with the torch axis were calculated to be 6 and 2° for internal and external injection, respectively. For internal injection, the deflection of the jet is noticeable when the carrier gas flow rate exceeds 10% of the plasma gas mass flow rate.

It should be noted that for internal injection of 22 to 45 μm alumina particles, the optimum carrier gas injection flow rate is 6 slm. This flow rate induces a relatively high deviation of the plasma jet. On the other hand, the optimum flow rate for external injection is only 4.5 slm. When the injector is moved further downstream, the carrier gas effect on the plasma jet becomes almost negligible.[18]

Figures 13(a) and (b) show the computed iso-values of velocity and temperature of the plasma jet for the highest carrier gas flow rate used in this study, *i.e.*, 8 slm. The effect of the transverse injection of the cold argon gas is not noticeable, although it amounts to a quarter of the argon plasma forming gas flow rate.

The effect of the carrier gas on the plasma flow was experimentally confirmed by measuring the profile and maximum value of the heat flux from the plasma jet to a water-cooled substrate perpendicular to the torch axis.[36] The computed deflection angles of the plasma jet for various carrier gas flow rates are in good agreement with the angles determined from calorimet-

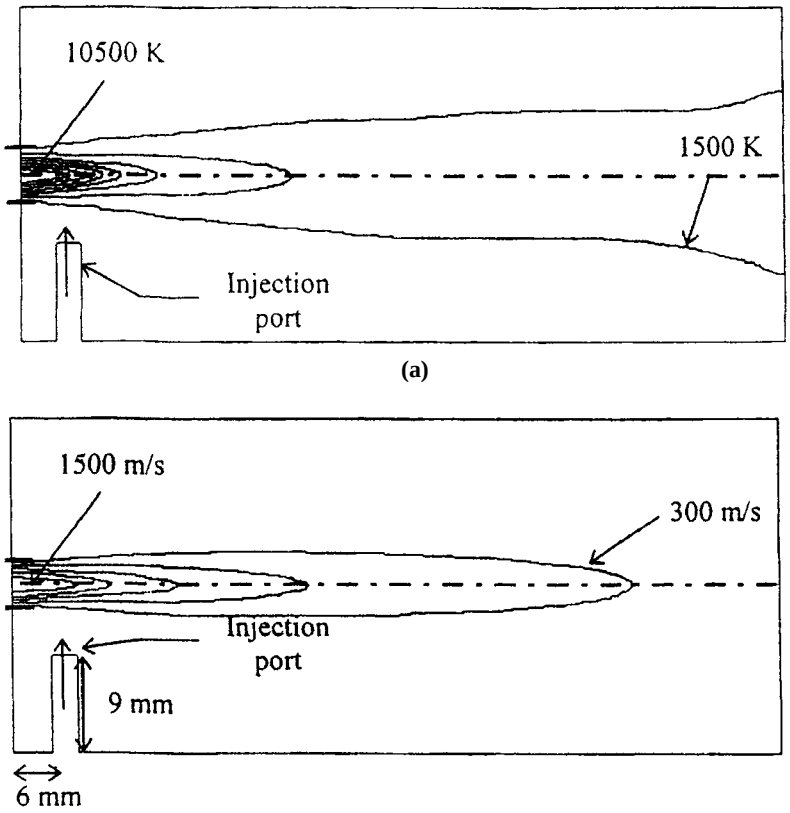

Fig. 13 (**a**) Isovelocity lines at intervals of 300 m/s; argon carrier gas flow rate: 8 slm, nozzle i.d.: 6 mm, P_{eff}: 13.5 kW, and plasma gas: 32 slm Ar + 12 slm H_2. (**b**) Isothermal lines at intervals of 1500 K; argon carrier gas flow rate: 8 slm, nozzle i.d.: 6 mm, P_{eff}: 13.5 kW, and plasma gas: 32 slm Ar + 12 slm H_2

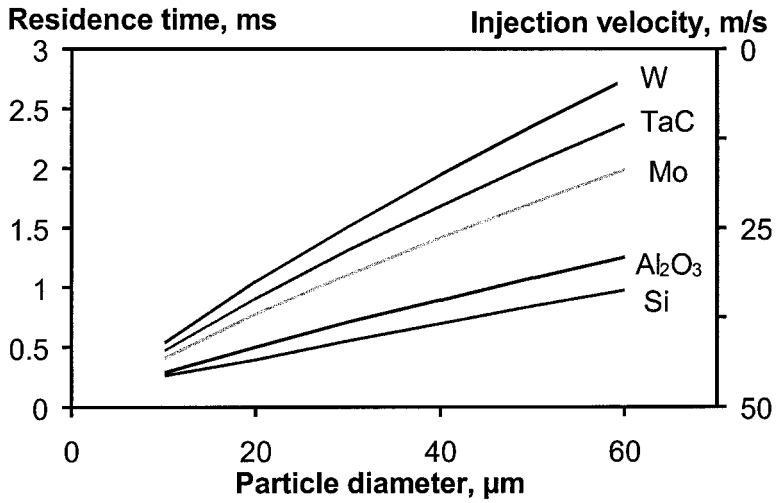

Fig. 14 Predicted particle residence time as a function of particle density and size (plasma forming gas: 45 slm Ar + 15 slm H_2, P_{eff}: 21.5 kW, and plasma gun i.d. 7 mm)

ric measurements. In Fig. 13(b), a colder zone surrounding the plasma jet at the nozzle exit can be observed for the internal injection. This zone is more pronounced at lower carrier gas flow rates. Such flow rates may result in poor penetration of the gas/powder jet in the plasma flow and consequent bypassing of particles.

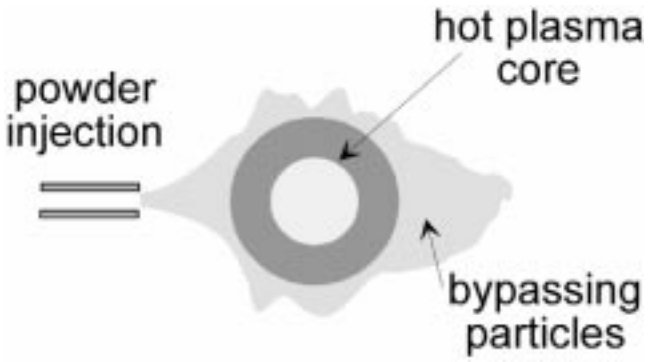

Fig. 15 Illustration of spatial distribution of particles bypassing plasma cone

4.5 Penetration of Injected Particles into the Plasma Jet

The particle injection parameters control to a large extent the particle trajectory, the dispersion of the powder in the plasma jet, and the deposition efficiency. The carrier gas flow must allow the maximum number of particles to penetrate into the plasma flow. The optimum mass flow of carrier gas depends on the injector diameter and location, the plasma jet momentum and the density, and the particle size distribution of the feed powder.

Vardelle *et al.*[3] have shown that when a particle is injected in the radial direction r through the periphery of the plasma jet, the total time of flight of the particle in the x axial direction is determined by the distribution of jet momentum within the jet cone envelope and a "reference time" group of the particles/plasma system that controls the advance of particles in the r direction. This reference time is defined as $\rho_p d_p^2/\mu_g$, where ρ_p and d_p are the particle density and diameter, respectively, and μ_g is the plasma gas viscosity. Calculations were performed for a plasma jet (Ar: 45 slm, H_2: 15 slm, plasma torch of 7 mm i.d., and power input in the gas 21.5 kW). The injector exit was located at the nozzle exit, 6.5 mm off the axis, and the stand-off distance was 100 mm. Figure 15 shows the computed residence time t_r for particles of different sizes and materials injected in a plasma jet of this configuration. The results show that the relationship between the particle diameter and material density is nearly the same as that represented by the reference time:

$$\frac{\rho_p d_p^2}{\mu_g} \qquad \text{(Eq 5)}$$

with the gas viscosity μ_g assumed to be constant. As noted above, this group corresponds to the reference time that controls the advance of the particle radially into the jet.[35]

Since the larger and denser particles are more resistant to the horizontal drag force, they spend more time in the plasma jet, which is favorable for the plasma spray process. However, for large particles of low density and low conductivity, the rate of heat conduction in the particles may be too slow to ensure homogeneous heating and melting during the residence time of the particles in the plasma jet. For example, experimental evidence has shown that, when spraying a zirconia powder with a particle size range of 10 to 106 μm, particles with a diameter less than 60 μm were not fully molten.[37]

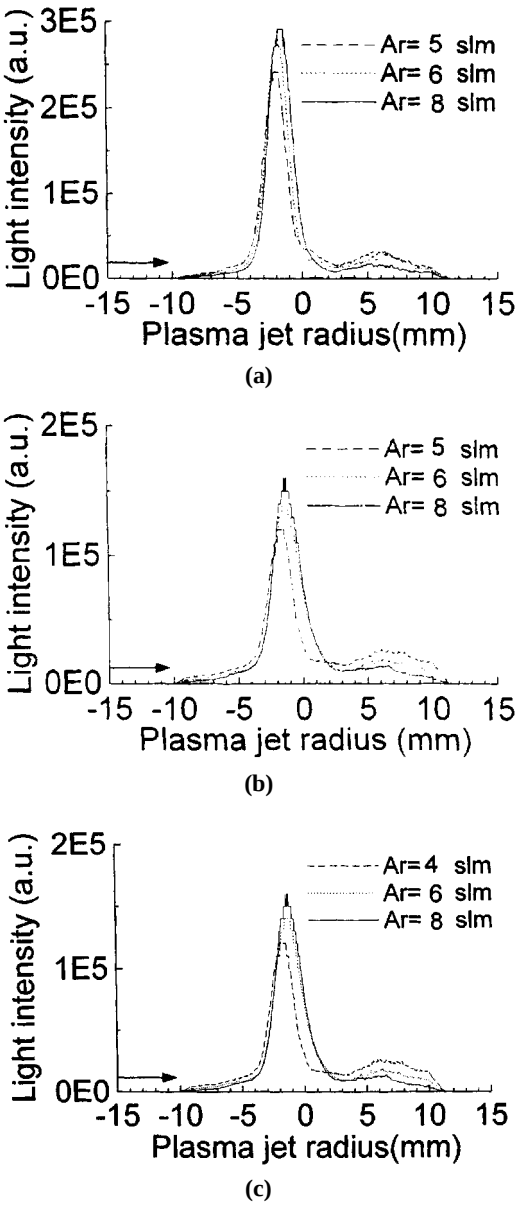

Fig. 16 Particle distribution profiles of Cr_2O_3 (5 to 22 μm, test 10, Table 1) sprayed by a SNMI torch (Fig. 3b): (**a**) x = 2 mm and (**b**) x = 5 mm. (**c**) Particle distribution profiles of ZrO_2 (5 to 45 μm, test 4, Table 1) sprayed by a LAB plasma gun and with powder injector at x = 10 mm

After determining that the residence times of various particles are a function of their density and diameter (Fig. 14), an equation expressing the radial distance traveled by these particles as a function of their injection velocities u_o was established.[35]

The required injection velocity varies with particle size and density in order for all particles to "land" on nearly the same spot on the substrate. By arbitrarily setting the radial direction r to be traveled by particles at 10 mm and by using this value in the force balance and the computed residence times of Fig. 14, the required injection velocities for each material and particle size were calculated. The results are plotted on the right-hand y-axis

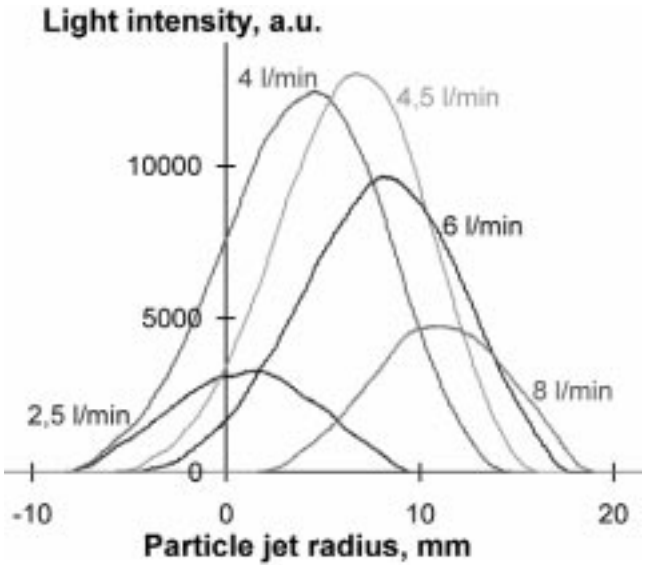

Fig. 17 Effect of carrier gas flow rate on the radial distribution of alumina powder (22 to 45 μm; test 9, Table 1; Ar 45 slm, H_2 15 slm, P_{eff} = 20 kW, and injector i.d. 1.75 mm)

of Fig. 14. This plot can be used to determine how the injection velocity should be changed to accommodate different particle sizes and materials.

Fine particles and especially those of low-density material require a high carrier gas flow rate to impart the appropriate velocity at the injection point.

4.6 Particles That Bypass Plasma Jet

It is evident that particles close to the periphery of the injection cone may bypass the plasma jet, as illustrated in Fig. 15. The amount will increase with radial distance of the injector tip from the axis of the plasma jet. However, if the tip is too close to the plasma cone, it will result in overheating and clogging, if not melting, of the injector tip.

Figure 16 shows the effect of the injection velocity on the amount of particle bypass for an injector located at an axial distance of 2 or 5 mm from the plasma torch exit. The sprayed particles were Cr_2O_3 powder and the plasma torch used was that shown in Fig. 3(b). The particle distribution along the diameter of the plasma jet was measured by using the light scattering technique described earlier. Both plots show that the principal maximum of each distribution profile is displaced toward the torch axis centerline as the carrier gas flow rate is increased from 5 to 8 slm. Also, the minor peak, at about 7 mm above the jet axis, is due to particles bypassing the plasma jet and distributing spatially over it, as illustrated in Fig. 15. The distribution profile for the 8 slm flow rate exhibits the highest primary peak and the least pronounced secondary peak, both of which denote a reduced amount of particle bypass.

Figure 16(b) shows that the secondary peaks are more pronounced for Ar flow rates of 5 to 6 slm and that the distributions of particles are fully asymmetrical for these two flow rates. Thus, for the same powder loading conditions, the change in carrier gas flow rate causes the main peak to increase with increasing flow

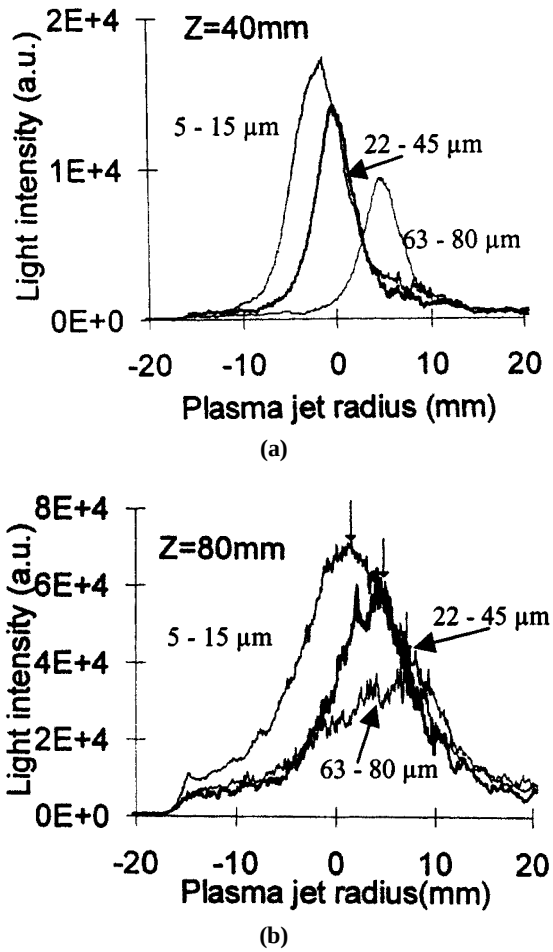

Fig. 18 Radial distribution profiles of ZrO_2 particle sprayed with the gun design of Fig 1(a) at (**a**) x = 40 mm and (**b**) x = 80 mm downstream of the nozzle exit for various size ranges (tests 1 to 3, Table 1); laser scattering measurements

rate. Similar results were obtained spraying ZrO_2 5 to 45 μm particles (Fig. 16c).

4.7 Particle Trajectory in Plasma Jet

Figure 17 shows the effect of carrier gas flow rate on the mean trajectory of a spray jet of alumina particles (test 9, Table 1) relative to the torch axis. Measurements were performed on hot particles at an axial distance of 70 mm from the plasma torch exit; the injection port was located 3 mm upstream of the nozzle exit (internal injection, Fig. 3a); the light signal was recorded over a time period of 0.4 ms. The curves exhibit a Gaussian shape and the particle trajectory and distribution shift with increasing injector gas flow rate.[38] The highest amplitude corresponds to a carrier gas flow rate of 4.5 slm, which is the optimal flow rate for the conditions of this test. The positions of the various trajectories vary by about 10 mm, corresponding to deviation angles (*i.e.*, the angle of mean particle trajectory with plasma axis) between 3 and 14˚. The integral of each distribution can be linked to a plasma/particle heat-transfer efficiency. If this efficiency is set equal to 1 at a carrier gas flow rate of 4.5

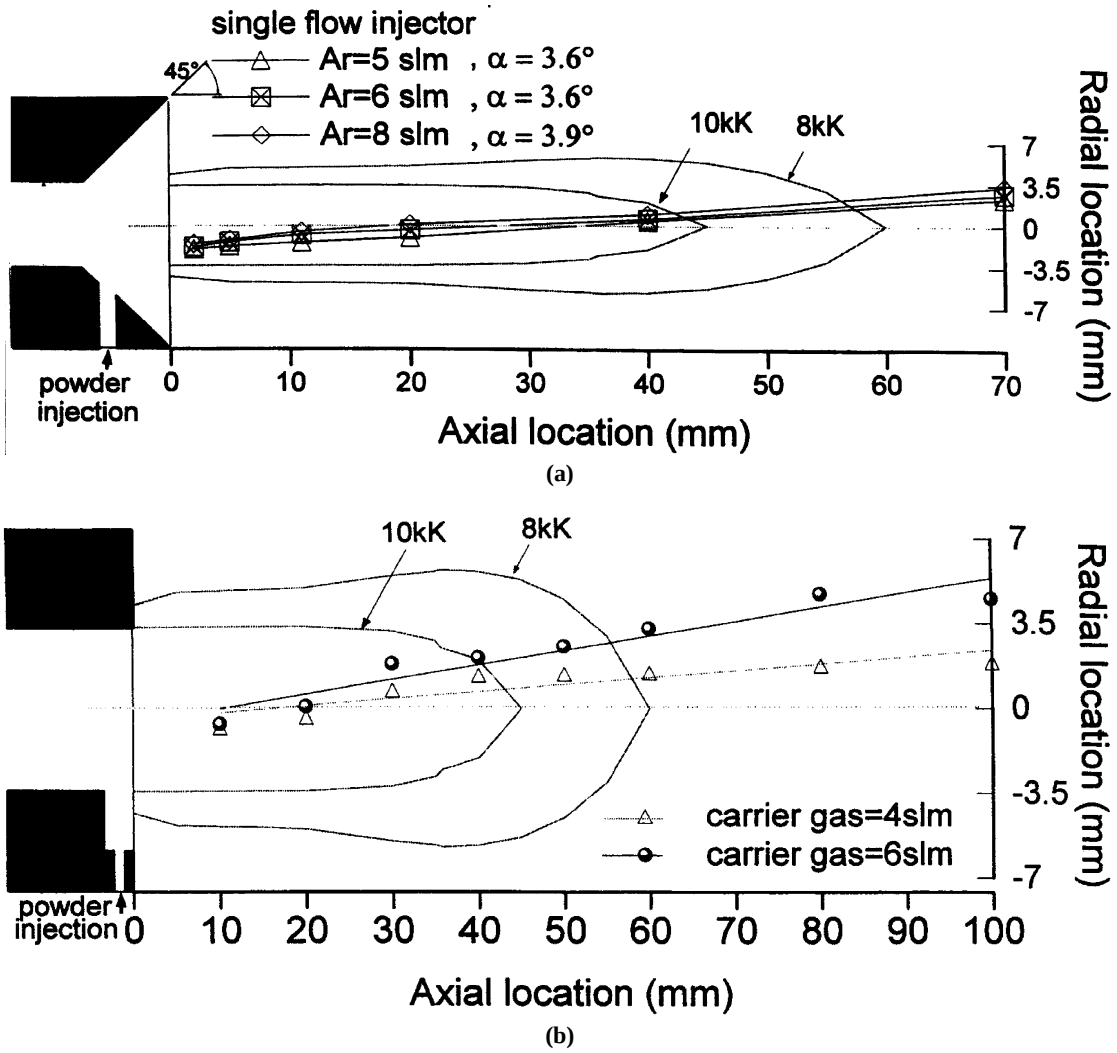

Fig. 19 (**a**) Mean Cr_2O_3 (5 to 22 μm, test 10, Table 1) sprayed with the gun design of Fig. 1(b). (**b**) Mean ZrO_2 (5 to 45 μm, test 4, Table 1) particle trajectories sprayed with the gun design of Fig 1(a)

slm, it is only 0.23 for 2.5 slm, 0.58 for 3 slm, and 0.73 for 6 slm. It should be noted that a variation of 10% in the carrier gas flow rate around the optimum value, 4.5 slm (for example, such as would be experienced if there was a gas leak), results in a decrease of 10% in heat-transfer efficiency.

Similar results were obtained with cold particles using the laser scattering technique described in Section 3.2. In this case, a second peak was observed due to particles bypassing the jet, especially those smaller than 20 μm in diameter. Figure 18 shows the signals obtained for zirconia particles of three sizes, at the same carrier gas flow rate. The plasma spraying conditions were the same as for Fig. 17.

Figure 18(a) shows that, as the mean particle size increases, the maximum of the distribution is displaced radially in the direction away from the injector. The gradual decrease in scattered light intensity is due to the fact that the signal intensity is related to the Mie scattering cross section and the number of particles. For the same loading rate of 1 kg/h, the larger size particles correspond to a smaller number of particles, and, in spite of the slight increase of the scattering cross section, the total scattered light is lower. Further downstream (Fig. 18b), the light signal of cold particles is more dispersed due to increased dispersion of the particle flow within the plasma jet and, also, peripheral entrainment by the jet of the small particles that initially bypassed the jet.[6]

For internal injection of particles, the mean trajectory of the fine particles does not change as the carrier gas flow rate increases from 5 to 8 slm (Fig. 19a) as noted earlier. As well, small particles experience many collisions with the injector wall and their velocity at the injector exit is nearly constant over a certain range of carrier gas flow rates. However, higher carrier gas flow rates may also deviate the jet flow; both effects result in the trajectories shown in Fig. 19(a).

The plasma flow deviation is confirmed by the observed decrease of "particle molten state" at the 8 slm carrier gas flow, as compared to the 5 slm flow. The molten state is determined by counting with image analysis the spherical particles collected along the mean trajectory at an axial distance of 150 mm from the plasma torch. With external injection, similar results were obtained except that the quantity of molten particles was practi-

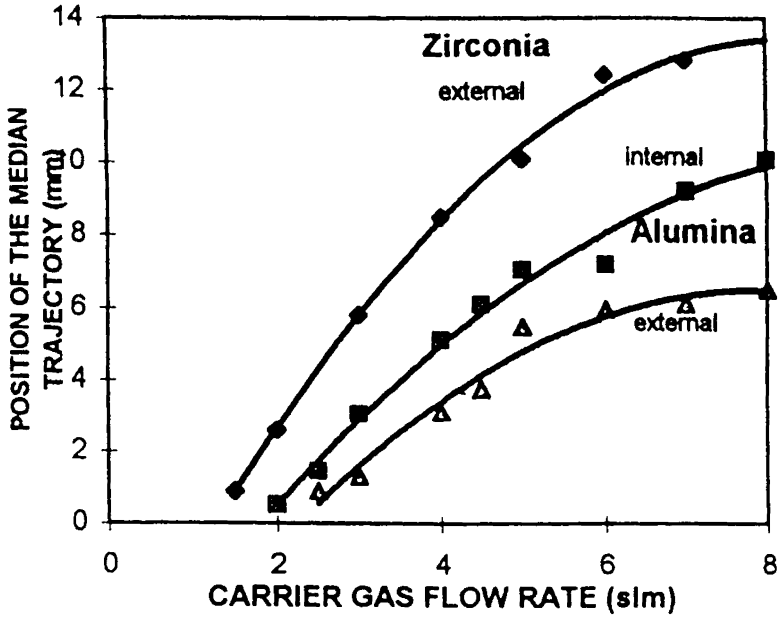

Fig. 20 Effect of injector location and carrier gas flow rate on particle median trajectory (tests 2 and 9, Table 1)

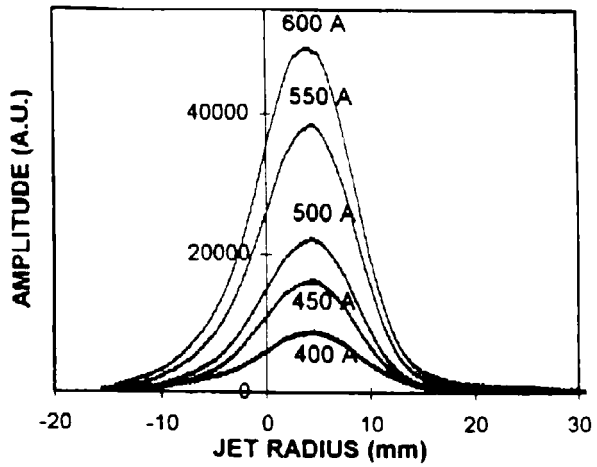

Fig. 21 Effect of arc current on radial distribution of alumina powder (test 9, Table 1)

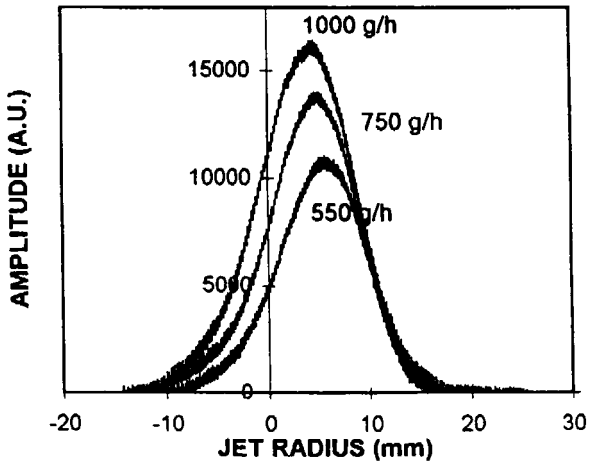

Fig. 22 Effect of powder mass flow rate on the radial distributions of alumina powder (test 9, Table 1)

cally insensitive to the carrier gas flow rate up to 8 slm. When considering larger particles (Fig. 19b), the mean trajectory is sensitive to the carrier gas flow rate, as would be expected from the results shown earlier (Fig. 17).

4.8 Effect of Internal or External Injection

Alumina and zirconia particles (22 to 45 μm, tests 2 and 9, Table 1) were injected in the same plasma jet (P_{eff} = 22.5 kW, 45 slm Ar, 15 slm H_2, and nozzle i.d. 7 mm) either internally (3 mm upstream of the nozzle exit, Fig. 3a) or externally (3 mm downstream of the nozzle exit).[38] The effect of injector location on mean particle trajectory is shown in Fig. 20 as a function of gas flow rate. The measurements were conducted at an axial distance of 70 mm from injector port.

The alumina powder was injected either internally or externally, while the zirconia powder was injected externally. At low carrier gas flow rates, the deviation of the particle trajectory from the jet axis increased almost linearly with gas flow rate. For values higher than 4.5 to 5 slm, a saturation of the light signals was observed. This was probably linked to plasma jet deformation due to the higher momentum of the cold carrier gas. The optimum heating of both powders corresponded to a radial position of the median trajectory ranging between 4 and 8 mm, at an axial distance at 70 mm from the injection point (for alumina powders, r = 4 to 6 mm). Due to the higher density of zirconia particles, and higher initial momentum at the same carrier gas velocity, there is a greater deviation in particle trajectory. This result is in good agreement with the computation results presented in Fig. 14.

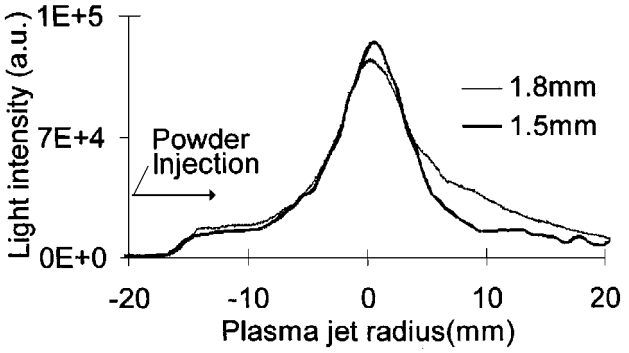

Fig. 23 Influence of injector internal diameter on particle distribution profile (measurements by laser scattering)

4.9 Effect of Arc Currrent

Figure 21 shows the light signals collected at a distance of 70 mm from the injection point for various arc currents; the carrier gas flow rate was 4.5 slm and alumina particles (test 9, Table 1) were injected into the plasma jet.

The light signals were very sensitive to the arc current level. Obviously, an increase in arc current results in more efficient heating of the spray jet; both particle temperature and the number of heated particles increase and augment the amplitude of the light signal. It has been estimated that a variation of 10% in arc current leads to a variation of 20% of the thermal efficiency criteria. The position of the maximum does not change with the arc current. This may be explained by a weakening of the turbulence level near the injection point. The turbulence zone moves forward with a current increase, and this balances the increase in plasma momentum with the current rise.

4.10 Effect of Powder Mass Flow Rate

When the powder feed rate is increased at fixed plasma conditions, the temperature and velocity in the plasma jet are reduced due to increased transfer of energy and momentum to the particles.[39] In addition, the particle velocities at the injector exit have less momentum. Therefore, the penetration of particles in the plasma jet is more difficult. Figure 22 shows a clear shift of 3 mm of the mean trajectory toward the torch axis. It can also be seen that, because of the lower temperature attained by the particles, the integrals of distributions corresponding to the mass flow rates of 550 and 1000 g/h do not differ by a factor of 2, as would have been expected if the particles were optimally heated.

4.11 Effect of Injector Internal Diameter

The data of Fig. 23 were acquired with two powder injectors of internal diameter 1.5 and 1.8 mm, respectively, under the same powder loading condition of 1 kg/h of zirconia (test 4, Table 1). The carrier gas flow rate was regulated at 3 slm for the 1.5 mm and 4 slm for the 1.8 mm injectors so that the injected particles would travel along the same average trajectory within the plasma jet in both cases. Figure 23 shows that the particle distribution profile obtained at an axial distance of 40 mm from the plasma torch exit for the 1.5 mm injector is more compact than the corresponding profile for the 1.8 mm injector. This implies that more particles bypassed the plasma jet when using the larger diameter injector.

4.12 Effect of Momentum of Plasma Jet

The plasma jet momentum depends on the mass flow rate of the plasma-forming gas and the plasma jet velocity. The first parameter depends on the total gas flow rate and the fraction of heavy gases (argon or nitrogen) within it; the low-density gases such as helium and hydrogen contribute little to the gas mass flow rate. The plasma velocity depends on the plasma column constriction within the anode nozzle. This constriction is a function of the relative diameter of the plasma column compared to that of the nozzle. The plasma column diameter increases with arc current and decreases with increasing fraction of He and, especially, amount of H_2 in the feed gas. Measurements by Planche *et al.*[40] for Ar-H_2 plasma jets and by Janisson *et al.*[41] for ternary mixtures of Ar-He-H_2 have shown that the plasma jet velocity varies, roughly, as the square root of the arc current, the inverse of the square of the nozzle internal diameter, and the gas mass flow rate to the power of about 0.2.

To illustrate the effect of the jet momentum on the particle injection, a ternary mixture was chosen, at different total flow rates and constituent gas fractions. The main advantage of a ternary mixture containing an appreciable amount of He (>30%) is that it increases the jet viscosity at temperatures over 10,000 K,[42] delays the entrainment of air, and lengthens the plasma core slightly. The powders were injected with a curved injector (Fig. 4) of radius of curvature 25.4 mm and length L = 70 mm. The injector was placed externally at an axial distance of 6 mm from the nozzle exit and a radial distance of 9 mm from its axis. The plasma torch nozzle i.d. was 6 mm. To examine the influence of the jet momentum, a light material, *i.e.*, alumina (test 9, Table 2), was injected. In order to test the influence of the mass flow rate, two total gas flow rates, 50 and 27 slm, were used at an arc current of 320 A. These conditions amounted to six different mass flow rates: 0.811, 0.803, 0.435, 0.434, 0.293, and 0.289 g/s.

The resulting[43] mean position of the spray pattern at x = 70 mm from the nozzle exit is shown in Fig. 24(a). For nearly the same mass flow rate, when the hydrogen concentration is increased by 2%, the plasma velocity decreases by 7%. Thus, for the same carrier gas mass flow rate, the penetration of particles in the jet is easier.

When the plasma gas mass flow rate decreases, the particle penetration also becomes easier. When comparing a ternary mixture with a classical Ar-H_2 mixture (Fig. 24b), penetration at the lower mass flow rates is easier, but since the velocity of the 50 slm ternary mixture is greater than that of the binary mixture, the particle penetration is more difficult. The effect of the arc current I is shown in Fig. 24(c). Since the jet velocity increases roughly as $\sqrt{I}$, an increase in I at constant mass flow rate makes particle penetration more difficult. The optimum injection can be determined as described earlier (Fig. 17).

4.13 Effect of Curved Injector

Figure 25[18] shows the dependence of the center of the spray pattern of hot particles on the carrier gas flow rate. The curves exhibit a maximum that corresponds to the "optimum" carrier

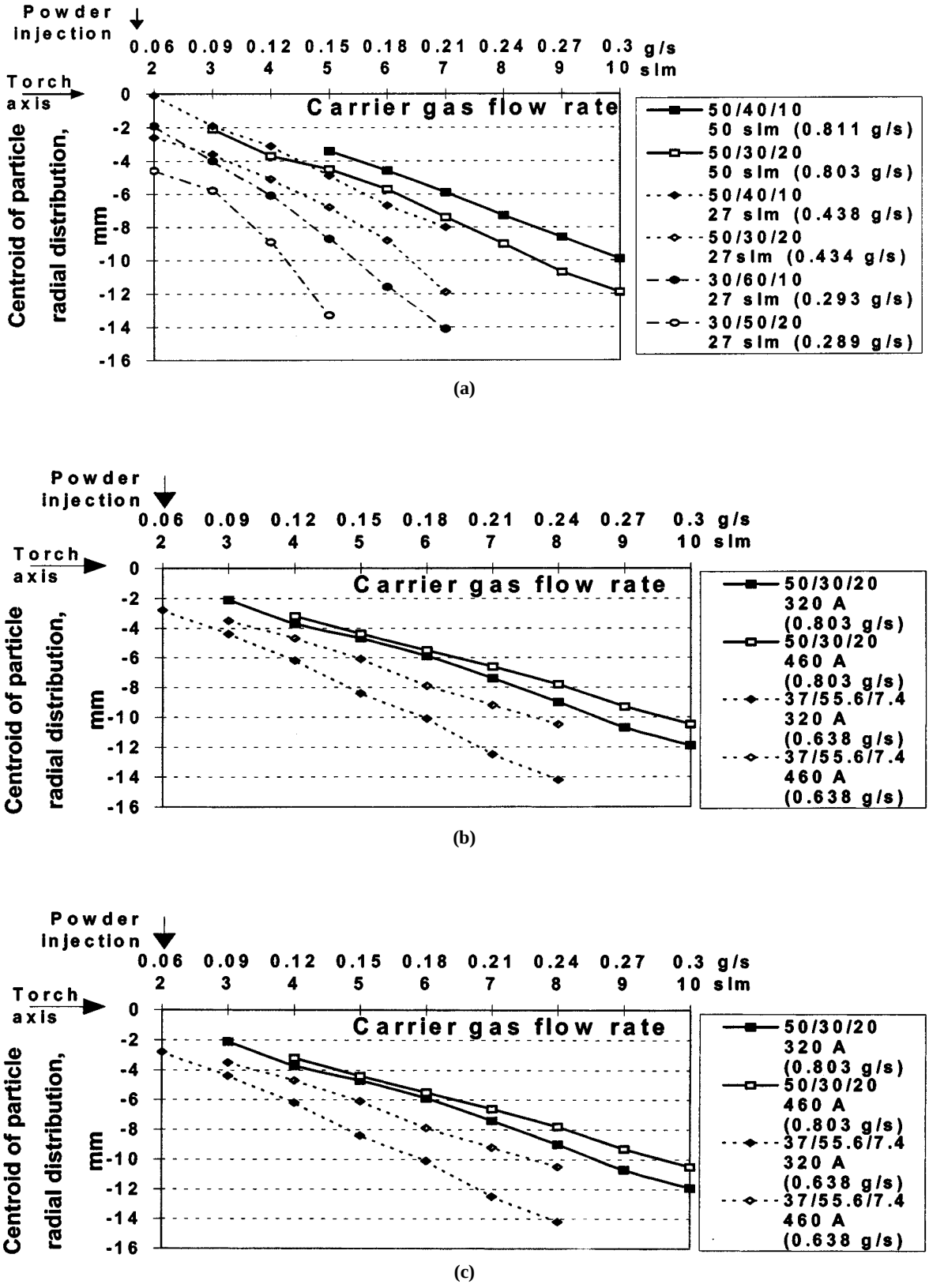

Fig. 24 Mean position from plasma axis of the spray pattern for alumina particles (test 9, Table 1) at x = 70 mm from plasma gun exit: (**a**) for different plasma mass flow rates and composition of the ternary Ar-H_2-He mixture and an arc current of 320 A; (**b**) for different ternary and binary gas mixtures, and (**c**) for two arc currents and two mass flow rates

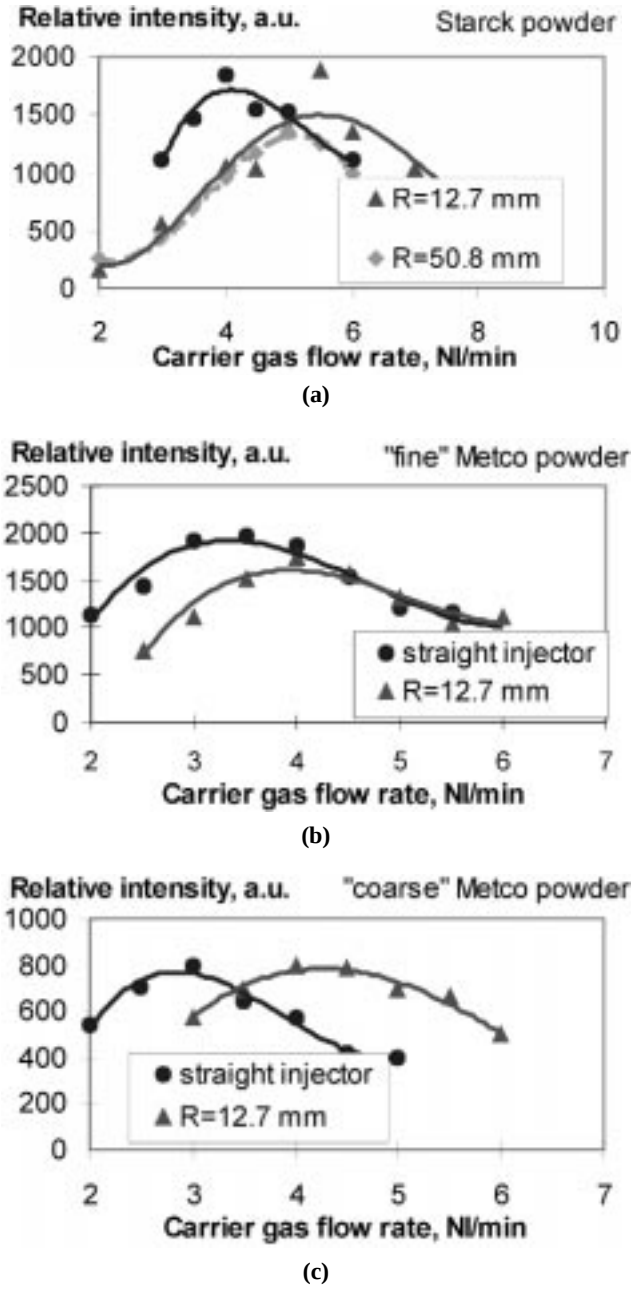

Fig. 25 Measured light maximum intensity vs carrier gas flow rate at 70 mm from the plasma gun exit, for different injector geometries: (**a**) Starck powder (test 2, Table 1), (**b**) Sulzer-Metco powder (test 5, Table 1), and (**c**) Sulzer-Metco powder (test 7, Table 1)

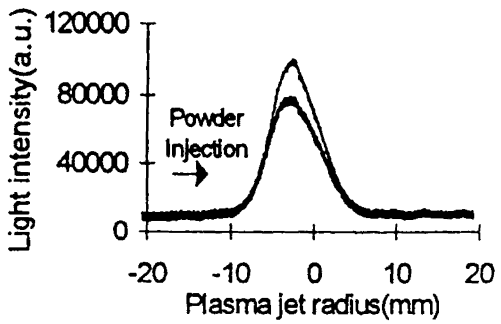

Fig. 26 Fluctuation of light signal with time at distance of 45 mm from injection point

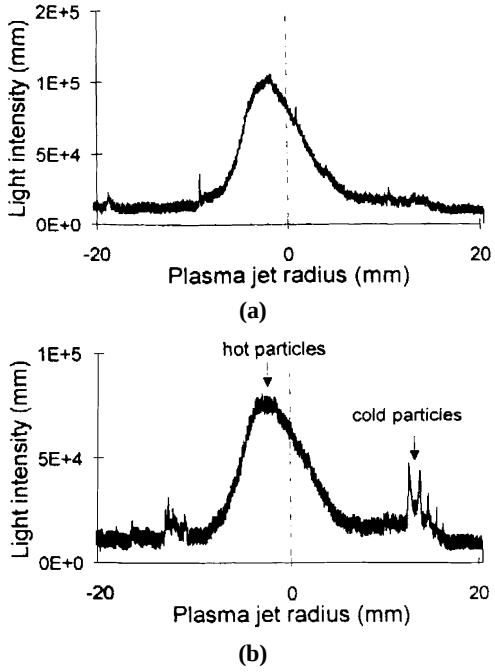

Fig. 27 Fluctuation of zirconia particle (22 to 45 μm) distribution profile; light signal composed of thermal emission from hot particles and scattering of laser light by all particles (recording at 45 mm from plasma gun exit at two different times)

gas flow rate under the conditions of the present study. This is defined as the gas flow rate resulting in most efficient heating and acceleration of particles. The optimum carrier gas flow rates for straight and various curved injectors are listed in Tables 4 and 5.

As would be expected from the earlier discussion of injector types, the carrier gas flow rate must be increased when using a curved injector, as compared to a straight one. The sharper is the curvature radius, the greater must be the carrier gas flow rate. In addition, it was observed that, for the fine zirconia powders (tests 2 and 5, Table 2), the light amplitude (measured from the diagnostic technique shown in Fig. 4) was lower with curved injectors. This can be explained by a larger spray pattern in the plasma jet. For a given carrier gas flow rate, the average particle size, size standard deviation, and morphology affect the penetration of the particles in the flow and the width of the spray pattern.

4.14 Influence of the Mode of Plasma Gas Injection

In a conventional plasma torch with a stick-type cathode, the plasma-forming gas is injected either longitudinally or with a small vortex. The plasma is excellent at disturbing any initial flow (*i.e.*, it can be described as a vortex killer[44]), and, therefore, no significant difference has been observed with or without vortex flow. However, this is not the case with high power ($P > 200$ kW) plasma torches where the strong vortex (vorticity < 20) in

Table 4 Dependence of the optimum carrier gas flow rate on injector geometry; Starck powder (test 2, Table 2)

	Optimal gas flow rate, slm, for Starck powder
Straight	4.2
R = 12.7 mm, L = 35 mm	5.7
R = 25.4 mm, L= 35 mm	5.4
R = 25.4 mm, L = 105 mm	5.4
R= 25.8 mm, L = 140 mm	5.7
R = 50.8 mm, L = 35 mm	5

Table 5 Dependence of optimum carrier gas flow rate on powder and injector geometry

Optimal gas flow rate, slm		Straight injector	R = 12.7 mm L = 35 mm
	Starck	4.2	5.7
Sulzer	Fine powder	3.25	4.2
Metco	Medium powder	3.7	4.0
	Coarse powder	2.85	4.3
	Ensemble	4.2	4.7

the injection chamber is not completely killed by the plasma flow. Such torches require a special geometry of powder injection.[45] The injector has to be adjusted with regard to the axis of the plasma torch and against the swirl direction, in order for the particle spray axis to coincide with the plasma plume.

5. Stability of Particle Injection

The short-term fluctuations (0.01 to 1 ms) of the particle injection are mainly due to the arc root fluctuations at the anode wall.[18,46,47] Typically, the frequency of the arc restrike mode of the arc root is about 10 to 20 kHz. High-speed pictures show that the plasma jet is fluctuating continuously both in position and length.[48] The voltage fluctuations for an Ar-H_2 plasma jet (45 slm Ar-15 slm H_2) operating at 600 A are up to 15% of the mean value. For a given arc current and plasma gas flow rate, this results in an enthalpy rate variation of 30%. Although the plasma temperature at the torch exit is not affected much, because gas ionization acts as a thermal inertia wheel,[35] the voltage fluctuations result in velocity fluctuations of the plasma jet momentum at any particular location. Accordingly, the particle mean trajectory also fluctuates over very short time intervals. This phenomenon has been verified by calculations.[35] Also, the light signals emitted or scattered by particles as they cross the laser sheet exhibit a large fluctuating component, on the order of 30% of the mean value. Figure 26 shows an example of two signals of hot particles recorded over a 13 ms interval.

Since the carrier gas flow rate is set on the basis of the plasma gas flow and average level of power dissipation, the particle trajectories correspond to the plasma jet fluctuation.[18] Therefore, the velocity and residence time of particles in the hot zone of the jet are also fluctuating. This contributes to the rather large distributions of particle velocities and temperatures observed upon impact on the substrate.[49]

Figure 27 shows the recorded light signals from laser light scattered by particles in the plasma jet and the emitted radiation from hot particles filtered at a wavelength of 514.5 nm. These distribution profiles were randomly sampled and integrated over 13 ms intervals at a location 45 mm downstream of the plasma torch exit. The difference between the two profiles (a) and (b) of Fig. 27 is attributed to the inherent fluctuation of the plasma jet. The two smaller peaks in Fig. 27(b), which occur at a radial distance of about 12 mm from the jet axis, arise mainly from fine particles that during the injection process did not have sufficient momentum from the carrier gas flow to penetrate into the plasma jet.

6. Conclusions

On the basis of this experimental and numerical study of powder injection in a plasma jet, the following conclusions can be drawn.

- The viscosity of the plasma gas does not play a major role in particle penetration in the jet, as shown by various experiments carried out with binary and ternary gas mixtures, whereas plasma jet momentum does.
- In the case of *internal injection* of the powder in the nozzle anode, the flow rate can induce a relatively high deviation of the plasma jet under conditions where the carrier gas exceeds 10% of the plasma gas mass flow rate.
- In the case of *external injection*, the carrier gas effect on the plasma jet is negligible.
- For a given carrier gas flow rate, the particle velocity at the injector exit is nearly independent of particle size; therefore, the finer particles may have insufficient momentum to penetrate the plasma jet and thus bypass it.
- The above bypass effect is more marked with injectors of larger diameter.
- For injectors of the same diameter, the carrier gas flow rate must be increased when using a curved injector, as compared to a straight one. The sharper is the curvature radius, the greater must be the carrier gas flow rate.
- The fluctuation of the arc root within the anode wall results in fluctuations in the particle spray jet; in turn, this results in a wider distribution of particle velocities and temperatures upon impact.

Overall, the parameters of particle injection in a plasma jet have a large effect on the shape and position of the particle spray jet and, thus, on particle acceleration, melting, and deposition efficiency. The optimum carrier gas mass flow rate depends on the injector diameter and positioning, plasma jet momentum, and size distribution and density of the feed material. In the mathematical modeling of the plasma spray process, the conditions of powder injection must be carefully chosen and represented in order for the model to project realistic particle trajectories. This remains a challenging problem, especially in three-dimensional models, where particle injection velocity, direction, and position in the injector must be fixed.

References

1. L. Pawlowski: *The Science and Engineering of Thermal Spray Coatings*, John Wiley & Sons, New York, NY, 1995.

2. P. Fauchais and M. Vardelle: *Pure Appl. Chem.*, 1994, vol. 66, pp. 1247-58.
3. J.R. Fincke, W.D. Swank, and C.L. Jefferey: *IEEE Trans. Plasma Sci.*, 1990, vol. 18, pp. 948-57.
4. M. Vardelle, A. Vardelle, A. Denoirjean, and P. Fauchais: *Materials Resesarch Society Symposia Proceedings*, MRS, Pittsburgh, PN, 1991, vol. 190, pp. 175-83.
5. M. Vardelle, A. Vardelle, and P. Fauchais: *Pure Appl. Chem.*, 1992, vol. 64 (5), pp. 637-44.
6. M. Vardelle, A. Vardelle, and P. Fauchais: *J. Thermal Spray Technol.*, 1993, vol. 2 (1), pp. 79-91.
7. M. Vardelle, A. Vardelle, P. Fauchais, and C. Moreau: *Meas. Sci. Technol.*, 1994, vol. 5, pp. 205-12.
8. M. Vardelle, A. Vardelle, A.C. Léger, and P. Fauchais: *J. Thermal Spray Technol.*, 1995, vol. 4 (1), pp. 50-58.
9. C. Moreau, P. Gougeon, and M. Lamontagne: *J. Thermal Spray Technol.*, 1995, vol. 4 (1), pp. 25-33.
10. M. Vardelle, A. Vardelle, K.I. Li, P. Fauchais, and N.J. Themelis: *Pure Appl. Chem.*, 1996, vol. 68 (5), pp. 1093-99.
11. C. Moreau, P. Gougeon, A. Burgess, and D. Ross: in *Advances in Thermal Spray Science and Technology*, C.C. Berndt and S. Sampath, eds., ASM International, Materials Park, OH, 1995, pp. 141-47.
12. P. Gougeon, C. Moreau, and F. Richard: in *Advances in Thermal Spray Science and Technology*, C.C. Berndt and S. Sampath, eds., ASM International, Materials Park, OH, 1995, pp. 149-55.
13. W.D Swank, J.R. Fincke, and D.C. Haggard: in *Advances in Thermal Spray Science and Technology*, C.C. Berndt and S. Sampath, eds., ASM International, Materials Park, OH, 1995, pp. 111-16.
14. K.-I. Li, M. Vardelle, and P. Fauchais: in *Advances in Thermal Spray Science and Technology*, C.C. Berndt and S. Sampath, eds., ASM International, Materials Park, OH, 1995, pp. 45-50.
15. L. Bianchi, A. Grimaud, F. Blein, P. Lucchese, and P. Fauchais: *J. Thermal Spray Technol.*, 1995, vol. 4 (1), pp. 25-33.
16. P. Fauchais, A.C. Léger, M. Vardelle, and A. Vardelle: *Proc. Julian Szekely Memorial Symp. on Materials Processing*, H. Y. Sohn, J.W. Evans, and D. Apelian, eds., TMS, Warrendale, PA, 1997, pp. 571-92.
17. L. Bianchi, A.C. Léger, M. Vardelle, A. Vardelle, and P. Fauchais: *Thin Solid Films*, 1997, vol. 305, pp. 35-47.
18. M. Vardelle, A. Vardelle, B. Dussoubs, P. Fauchais, T.S. Roemer, R.A. Neiser, and M.F. Smith: in *Thermal Spray: Meeting the Challenges of the 21st Century*, C. Coddet, ed., ASM International, Materials Park, OH, 1998, pp. 887-94.
19. J.R. Fincke, W.D. Swank, D.C. Haggard, T.M. Demeny, S.M. Pandit, and A.R. Kashani: in *Advances in Thermal Spray Science and Technology*, C.C. Berndt and S. Sampath, eds., ASM International, Materials Park, OH, 1995, pp. 117-22.
20. J.R. Fincke, W.D. Swank, D.C. Haggard, T.M. Demeny, S.M. Pandit, and A.R. Kashani: in *Advances in Thermal Spray Science and Technology*, C.C. Berndt and S. Sampath, eds., ASM International, Materials Park, OH, 1995, pp. 123-28.
21. J.R. Fincke, W.D. Swank, and D.C. Haggard: in *Thermal Spray: A United Forum for Scientific and Technological Advances*, C.C. Berndt, ed., ASM International, Materials Park, OH, 1997, pp. 335-42.
22. J.D. Mattei and O. Simonin: Logiciel ESTET. Manuel théorique de la version 3.1-Tome 1, Modélisations physiques, Rapport EDF No. HE 44/92.38B, 1992. EDF-LNH, 6 quai Watier, 78400 Chatou (in French).
23. J.D. Mattei and M. Ouraou: Descriptif informatique du code ESTET-version 3.1-Rapport EDF No. HE 44/93.20, 1992. EDF-LNH, 6 quai Watier, 78400 Chatou, France (in French).
24. B. Dussoubs B., P. Fauchais, A. Vardelle, M. Vardelle, and N.J. Themelis: in *Thermal Spray: A United Forum for Scientific and Technological Advances*, C. C. Berndt, ed., ASM International, Materials Park, OH, 1997, pp. 557-65.
25. B. Dussoubs, A. Vardelle, M. Vardelle, and P. Fauchais: *High Temp. Mater. Processes*, 1997, vol. 3.
26. M. Leylavergne, A. Vardelle, B. Dussoubs, and N. Goubot: in *Thermal Spray: A United Forum for Scientific and Technological Advances*, C.C. Berndt, ed., ASM International, Materials Park, OH, 1997, pp. 459-65.
27. B.E. Launder and B.I. Sharma: *Computer Methods Appl. Mech. Eng.*, 1974, vol. 3, pp. 269-89.
28. J.P. Padet: *Flowing Fluids, Methods and Models*, Masson, Paris, 1991 (in French).
29. B. Dussoubs, A. Vardelle, K.I. Li, M. Vardelle, and P. Fauchais: *12th Int. Symp. on Plasma Chemistry*, J.V. Heberlein, T.W. Ernie, J.T. Roberts, eds., Minneapolis, MN, 1995, vol. 3, pp. 1343-49.
30. K.-I. Li.: "Contribution to the Study of Particle Injection and Vaporization in d.c. Plasma Spray Jets," Ph.D. Thesis, University of Limoges, Limoges, Mar. 1998 (in English).
31. G.E. Klinzing: *Gas-Solid Transport*, McGraw-Hill, New York, NY, 1981, pp. 109-21.
32. P. Proulx: "Mathematical Modeling of Plasma-Particles Flow," Ph.D. Thesis, University of Sherbrooke, Sherbrooke, PQ, Canada, July 1987 (in French).
33. B. Dussoubs, A. Vardelle, M. Vardelle, and P. Fauchais: *Proc. 4th Thermal Plasma Processes Conf.*, Athens, Greece, July 15-18, 1996, P. Fauchais, ed., Begell House, New York, NY.
34. C.H. Chang and J.D. Ramshaw: *Plasma Chem. Plasma Proc.*, 1996, vol. 16, pp. 5S-17S.
35. A. Vardelle, P. Fauchais, B. Dussoubs, and N.J. Themelis: *Plasma Chem. Plasma Proc.*, 1998, vol. 18 (4), pp. 551-78.
36. F. Monerie-Moulin, F. Gitzhofer, P. Fauchais, M. I. Boulos, and A. Vardelle: *J. High Temp. Chem. Proc.*, 1992, vol. 1 (3), pp. 249-57.
37. A.C. Léger: "Contribution to the Experimental Study of Zirconia Splats, Their Piling Up and Their Cohesion and of Residual Stresses in Plasma Sprayed Coatings," Ph.D. Thesis, University of Limoges, Limoges, Mar. 1997 (in French).
38. M. Vardelle, P. Fauchais, A. Vardelle, and A.C. Léger: in *Thermal Spray: A United Forum for Scientific and Technological Advances*, C.C. Berndt, ed., ASM International, Materials Park, OH, 1997, pp. 535-42.
39. A. Vardelle, M. Vardelle, P. Fauchais, P. Proulx, and M.I. Boulos: in *Thermal Spray: International Advances in Coatings Technology*, C.C. Berndt, ed., ASM International, Materials Park, OH, 1992, pp. 543-47.
40. M.P. Planche, J.F. Coudert, and P. Fauchais: *Plasma Chem. Plasma Proc*, 1998, vol. 18 (2), pp. 263-74.
41. S. Janisson, E. Meillot, A. Vardelle, J. F. Coudert, B. Pateyron, and P. Fauchais: in *Thermal Spray: Meeting the Challenges of the 21st Century*, C.Coddet, ed., ASM International, Materials Park, OH, 1998, pp. 803-08.
42. J.M.Léger, P. Fauchais, A. Grimaud, M. Vardelle, A. Vardelle, and B. Pateyron: in *Thermal Spray: International Advances in Coatings Technology*, C.C. Berndt, ed., ASM International, Materials Park, OH, 1992, pp. 17-20.
43. S. Janisson, A. Vardelle, M. Vardelle, P. Fauchais, and E. Meillot: *Proc. 5th Thermal Plasma Processes Conf.*, St Petersburg, Russia, July 1998, P. Fauchais, ed., Begell House.
44. Y.P. Chyon and E. Pfender: *Plasma Chem. Plasma Proc*, 1989, vol. 9 (2), pp. 291-341.
45. W.D. Swank, C.H. Chang, J.R. Fincke, and D.C. Haggard: in *Thermal Spray: Practical Solutions for Engineering Problems*, C.C. Berndt, ed., ASM International, Materials Park, OH, 1996.
46. J.F. Coudert and P. Fauchais: *J. High Temp. Mater. Processes*, 1997, vol. 2, pp. 149-65.
47. P. Fauchais, J.F. Coudert, and M. Vardelle: *J. Phys. IV*, 1997, vol. 7, pp. 187-98.
48. M.P. Planche: "Contribution to the Study of Fluctuations in a d.c. Plasma Torch. Application to the Arc Dynamic and to the Flow Velocity," Ph.D. Thesis, University of Limoges, Limoges, May 1995 (in French).
49. J.R. Fincke, W.D. Swank, C.L. Jefferey, and C.A. Manusev: *Meas. Sci. Technol.*, 1993, vol. 4, p. 559.